Robotica (2018) volume 36, pp. 1402–1420. © Cambridge University Press 2018
doi:10.1017/S0263574718000383

A vibration-driven planar locomotion robot—*Shell*

Xiong Zhan, Jian Xu*, Hongbin Fang

School of Aerospace Engineering and Applied Mechanics, Tongji University, Shanghai 200092, P. R. China. E-mails: 90zhanxiong@tongji.edu.cn, fanghongbin@tongji.asia

(Accepted April 28, 2018. First published online: June 13, 2018)

SUMMARY

This paper reports the design, analysis, and control of a miniature vibration-driven planar locomotion robot called *Shell*. A vibration-driven system is able to achieve locomotion based on internal oscillations and anisotropic friction forces. In this robot design, two parallel oscillators are employed to provide propelling forces, and a blade-like support is designed to generate anisotropic frictional contact with the ground. If the two parallel oscillators are of different frequencies and amplitudes, two-dimensional locomotion of the robot can be achieved. To predict the robot's planar locomotion, a dynamic model is developed. Controlling the robot's locomotion and especially, the locomotion modes can be achieved by adjusting the vibration frequencies of the two internal oscillators. Experimental results show that *Shell* can be controlled to move rectilinearly and along circles with certain curvatures. In addition, by combining these basic trajectories, *Shell* can move freely on a horizontal plane.

KEYWORDS: Bioinspired robot, Miniature robot, Robot locomotion, Planar trajectory, Electromagnetic actuation, Anisotropic friction.

1. Introduction

The prototype *Shell* reported in this paper belongs to miniature locomotion robots. This class of robots has high mobility and flexibility in limited spaces,[1,2] which enables them to have potential applications in pipeline inspection, disaster rescue, reconnaissance in battle fields, etc. Learning from the animal's locomotion, especially snakes,[3] earthworms,[4] caterpillars,[5] inchworms,[6] and cockroaches,[7] provides us with important guidelines for modelling miniature robots. The mechanical model of *Shell* presented here is a vibration-driven locomotion system, which is often adopted to build earthworm-like robots.[8–12] The vibration-driven locomotion system can move in resistive medium without complex transmission systems or protruded active components, such as legs, wheels, and tentacles; therefore, they are relatively simple in design, possess high miniaturization potential, and have promising applications in various environments ranging from narrow crevices to strongly corrosive surroundings.

Vibration-driven locomotion systems have been widely investigated from various aspects including single-module and multi-module system modelling,[10,12,13] steady-state motion analysis,[12,13] locomotion optimization,[9,14] introducing nonlinearities into the internal actuation,[15] designing, prototyping,[16–18] etc. In these studies, internal drives and external friction have been recognized as the two key factors in generating locomotion of the systems. The internal drives provide the power, which are transformed into the net displacement of the overall system providing that it works in a resistant medium.

Various methods have been proposed to actuate the internal drives, including DC-motor-driven pendulum,[16] electromagnetic mechanisms,[17] vibration-impact mechanisms,[18] bioinspired muscle-like mechanism,[19] etc. The development of locomotion systems has also expanded to the 2D scope. The manoeuvrability is an important feature for locomotion robots. Up to now, many scholars have figured out a variety of ways to produce turning motion for locomotion robots. Among them, many are inspired by the locomotion of animals. For snake-like robots, DC servo motors are used to provide the rotation

* Corresponding author. E-mail: xujian@tongji.edu.cn

https://doi.org/10.1017/S0263574718000383 Published online by Cambridge University Press

angle between body segments of the robots.[20,21] To realize a hexapod-like locomotion, Zarrouk[22] used one motor to swing six compliant legs. By exploiting the stiffness disparity of the six legs, different advances of the sides of the insect-like robot is generated and then yaw rotation is realized. In contrast, to achieve the advance difference between the two sides of robots, the earthworm-like plane robot proposed by Song[23] turns in a different way. Each of its body segments has two solenoid actuators and the angular displacement is produced by the unsynchronized motion of the solenoid pair. Arai[24] achieved this in a similar way by changing the length of elastic rods. From the above works, one may find that to perform planar locomotion, there should be an advance disparity between the two sides of locomotion robots. However, no such work has been seen in the planar locomotion realization of vibration-driven systems.

On the other hand, the resistance force is also necessary for vibration-driven locomotion. Particularly, the resistance force is always assumed to be anisotropic, i.e., the resistance force for forward locomotion is lower than that for backward locomotion.[8,25] The introduction of anisotropic dry friction could induce stick-slip motion of the vibration-driven systems, which has been found in both single-module and multi-module systems.[26] In the single-module system, through classical mechanics method[13] and sliding bifurcation method,[25] the stick-slip motions are qualitatively classified. Moreover, it has been discovered that stick-slip effect can be utilized to optimize the system's locomotion. The classification makes it possible to adjust actuation parameters such that the system can achieve directional locomotion without backward slip, and the overall steady-state velocity can be improved. An extreme case of the anisotropic friction is that the backward friction is large enough such that the backward motion of the system is completely restrained. Such state is always referred to as anchoring. Anchoring can be realized, experimentally, by adopting bristle structures[12,27] or through segment expansion.[19]

In this paper, a miniature robot *Shell* is modelled and fabricated based on a vibration-driven system. To achieve its planar locomotion, two internal masses vibrate sinusoidally in two parallel laid grooves, respectively. When the two internal masses vibrate in exactly the same way, the robot would be actuated to move in a straight line along its initial direction. However, when the motion laws of the two internal masses are distinct from each other, the robot would probably be actuated to turn due to the different interaction forces imposed on the robot by the two internal masses. In this way, the advance disparity of the two sides of the minirobot *Shell* is produced and planar trajectories would be performed. This is the idea that how the vibration-driven system can perform planar locomotion in the paper.

The remainder of the paper is arranged as follows. In Section 2, the dynamic model of *Shell* is established, based on which some analytical properties about the planar locomotion of *Shell* is demonstrated; a detailed description and a discussion of the two key factors, internal actuations and external anisotropic dry friction, are given in Section 3; Section 4 illustrates the setup of the experiment and various trajectories *Shell* may perform. In Section 5, main contributions of the paper are summarized and concluded.

2. Modelling of the Vibration-Driven Planar Locomotion System

2.1. System configuration

The vibration-driven locomotion system considered here consists of a rectangle rigid body M as a carrier and two internal masses (m_1 and m_2) acting as actuators, as shown in Fig. 1(a). To describe locomotion trajectory and geometry dimensions of the dynamical system, two coordinate systems are introduced, i.e., an inertial coordinate system $oxyz$ and a moving coordinate system $\xi o_1 \eta$ fixed to body M with its origin o_1 at the centre and its coordinate axes along symmetric axes of body M. Coordinate θ denotes the angle from the positive x -axis to the positive ξ -axis, i.e., the orientation of body M. Two grooves (shown in shadow), within which two masses m_1 and m_2 move periodically relative to the carrier M, are reflection-symmetric about axis ξ, and the distance from each groove to the axis ξ is b. One support, denoted by C_i (i =1, 2, 3, 4), is equipped at each corner of body M, providing anisotropic Coulomb dry friction. Distances from support C_i (i =1, 2, 3, 4) to axis ξ and axis η are d and a, respectively.

The motion of vibration-driven systems is determined by its internal drive and external friction, which act as active and resistant forces, respectively. From the study of the single-DOF vibration-driven system,[17] it is known that for the simple harmonic internal drive, the system cannot have periodic net

https://doi.org/10.1017/S0263574718000383 Published online by Cambridge University Press

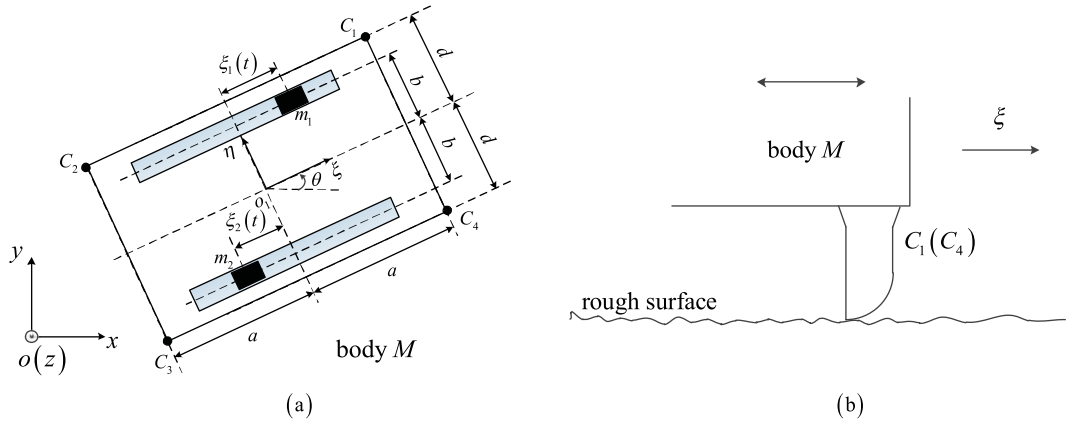


Fig. 1. (a) Dynamical model of the vibration-driven locomotion system. (b) Support used to provide anisotropic dry friction.

displacement unless the external friction is anisotropic. Furthermore, anisotropic friction coefficients are usually utilized to optimize the rectilinear motion of vibration-driven systems subject to various types of friction, such as dry friction[8,10] and viscous friction.[13] This is why anisotropic friction is popular in the studies of the rectilinear motion of vibration-driven systems. Due to these advantages, friction anisotropicity (Goal #1) is retained in modelling a vibration-driven planar locomotion robot in the paper. For planar locomotion (Goal #2), it is required that the robot can not only move forward and backward but also turn clockwise and anticlockwise, which calls for higher demand in manoeuvrability. However, herein friction anisotropicity is only supposed to exist along the ξ -axis. Our idea is that the planar locomotion model can be modelled as simple as rectilinear ones in terms of anisotropic friction and can be actuated to move freely on a horizontal plane. To achieve Goal #1, the support C_i (i =1, 2, 3, 4) of the system is designed, as shown in Fig. 1(b). Here, we have some remarks on the supports:

1. The supports are regarded as rigid for their shortness.
2. Friction anisotropicity is always along the local coordinate axis ξ, i.e., the direction to which the system is heading, while the horizontal supporting plane is isotropic.
3. Dry friction coefficient for forward motion is assumed to be smaller than that for backward motion.

2.2. Dynamic model and planar locomotion mechanisms

The dynamical model of the planar locomotion of the system shown in Fig. 1 is given in Eq. (1). For the details of the governing equation and the anisotropic friction acting on the system, please see the Appendix:

$$\begin{cases} \sum_{j=0}^{2} m_j \ddot{x} - \sum_{j=1}^{2} m_j \left(\xi_j \sin\theta + B_j \cos\theta\right) \ddot{\theta} - \sum_{j=1}^{2} m_j \left(\xi_j \cos\theta - B_j \sin\theta\right) \dot{\theta}^2 - 2 \sum_{j=1}^{2} m_j \dot{\xi}_j (\sin\theta)\dot{\theta} + \sum_{j=1}^{2} m_j \ddot{\xi}_j \cos\theta = Q_x \\ \sum_{j=0}^{2} m_j \ddot{y} - \sum_{j=1}^{2} m_j \left(-\xi_j \cos\theta + B_j \sin\theta\right) \ddot{\theta} - \sum_{j=1}^{2} m_j \left(\xi_j sin\theta + B_j \cos\theta\right) \dot{\theta}^2 + 2 \sum_{j=1}^{2} m_j \dot{\xi}_j (\cos\theta)\dot{\theta} + \sum_{j=1}^{2} m_j \ddot{\xi}_j \sin\theta = Q_y, \\ \sum_{j=1}^{2} m_j \left(-\xi_j \sin\theta - B_j \cos\theta\right) \ddot{x} + \sum_{j=1}^{2} m_j \left(-B_j \sin\theta + \xi_j \cos\theta\right) \ddot{y} + \left(J + \sum_{j=1}^{2} m_j \left({\xi_j}^2 + {B_j}^2\right)\right) \ddot{\theta} + 2 \sum_{j=1}^{2} m_j \xi_j \dot{\xi}_j \dot{\theta} - \sum_{j=1}^{2} m_j \ddot{\xi}_j B_j = M_\theta \end{cases} \tag{1}$$

where the generalized force Q_x is the Coulomb dry friction body M subject to in the x direction, Q_y that in the y direction, and M_θ the resistant moment with its positive direction anticlockwise.

At this point, we have a remark on the governing Eq. (1). It is almost the same to the one in ref. [28] except the dry friction force and torque. In this paper, dry friction is considered. Furthermore, Volkova *et al*. achieve planar locomotion by adjusting the tilt angles of the supports and internal drives by assuming that the driving amplitudes and frequencies of the two internal drives are identical. However, planar locomotion discussed here is realized by two different driving forces such that a turning torque

https://doi.org/10.1017/S0263574718000383 Published online by Cambridge University Press

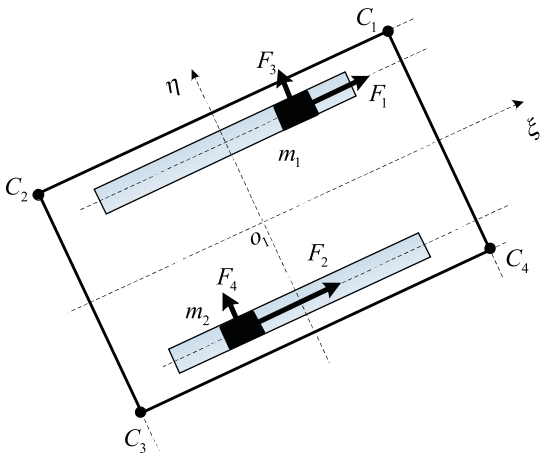


Fig. 2. Force analysis of the system; F_1 and F_2 are forces caused by the relative motions of the internal masses; F_3 and F_4 are active forces caused by the rotation of body M.

will be imposed on the system. In this way, a turning motion of the robot is produced. Figure 2 shows the forces propelling the robot to move and to rotate. F_1 and F_2 are forces caused by the relative motion of the internal masses m_1 and m_2, respectively. F_3 and F_4 are forces caused by the rotation of body M. It is easy to see that body M is actuated to rotate by the resultant torque of forces F_1, F_2, F_3, and F_4 with respect to the mass centre of the system. Thus, to control the rotation of body M, one can simply adjust parameters of the internal drives $\xi_1(t)$ and $\xi_2(t)$.

Up to now, governing equation of the locomotion of the robot is derived. However, Eq. (1) is complex, and it is hard to see the motions it implies. Thus, in the following content, the governing equation is converted to the form expressed in the natural coordinates, based on which qualitative properties about the system are given.

To show progressive and turning motions of the considered system clearly, it is necessary to transform the governing Eq. (1) into the form expressed in natural coordinates, i.e., s along the tangential of the planar trajectory, n perpendicular to the trajectory, and θ the angle to the positive x-axis. It is known that

$$\begin{pmatrix} \ddot{s} \\ \ddot{n} \end{pmatrix} = {T_r}^{-1} \begin{pmatrix} \ddot{x} \\ \ddot{y} \end{pmatrix} \quad \text{and} \quad \begin{pmatrix} \dot{s} \\ \dot{n} \end{pmatrix} = {T_r}^{-1} \begin{pmatrix} \dot{x} \\ \dot{y} \end{pmatrix}, \tag{2}$$

where

$${T_r}^{-1} = \begin{pmatrix} \cos\theta & \sin\theta \\ -\sin\theta & \cos\theta \end{pmatrix}. \tag{3}$$

Thus, premultiplying the first two equalities in Eq. (1) by ${T_r}^{-1}$ and combining the third equality in Eq. (1) yield

$$\begin{cases} (M+2m)\,\ddot{s} + m\left(\ddot{\xi}_1 + \ddot{\xi}_2\right) - m\dot{\theta}^2\left(\xi_1 + \xi_2\right) = Q_\xi \\ (M+2m)\,\ddot{n} + 2m\left(\dot{\xi}_1 + \dot{\xi}_2\right)\dot{\theta} + m\left(\xi_1 + \xi_2\right)\ddot{\theta} = Q_\eta \\ \left(J + \sum\limits_{j=1}^{2} m_j\left(\xi_j^2 + B_j^2\right) - \frac{m}{M+2m} m(\xi_1+\xi_2)^2\right)\ddot{\theta} + \frac{\mathrm{d}}{\mathrm{d}t}\left(J + \sum\limits_{j=1}^{2} m_j\left(\xi_j^2 + B_j^2\right) - \frac{m}{M+2m} m(\xi_1+\xi_2)^2\right)\dot{\theta} \\ = mb\left(\ddot{\xi}_1 - \ddot{\xi}_2\right) + M_\theta - \frac{m}{M+2m}\left(\xi_1+\xi_2\right)Q_\eta \end{cases} \tag{4}$$

This is the planar locomotion of the vibration-driven system expressed in natural coordinates. From Eq. (4), it is easy to tell the progressive motion (s), the lateral motion (n), and the turning motion (θ) of the vibration-driven system. For the details of resistance forces (Q_ξ and Q_η) and torque (M_θ), please

https://doi.org/10.1017/S0263574718000383 Published online by Cambridge University Press

refer to Eqs. (A17)–(A19) in the Appendix. With Eq. (4), planar locomotion of the vibration-driven system is, to some extent, decoupled. In the following content, the three kinds of motions will be analysed one by one.

2.2.1. Progressive motion. In Eq. (4), the equation describing progressive motion is

$$(M+2m)\,\ddot{s}+m\left(\ddot{\xi}_1+\ddot{\xi}_2\right)-m\dot{\theta}^2\left(\xi_1+\xi_2\right)=Q_\xi. \tag{5}$$

In Eq. (5), there is a quadratic term of the angular velocity $\dot{\theta}$. It implies that the sign of angular velocity of body M makes no difference to the motion in the s direction. That is to say, the turning motion of the system is symmetric. Besides, if the term $m\dot{\theta}^2(\xi_1+\xi_2)$ induced by the system rotation is small compared to the driving term $m(\ddot{\xi}_1+\ddot{\xi}_2)$ so that it can be neglected, then Eq. (5) is reduced to

$$(M+2m)\,\ddot{s}+m\left(\ddot{\xi}_1+\ddot{\xi}_2\right)=Q_\xi. \tag{6}$$

Equation (6) agrees with the dynamic model proposed in the previous vibration-driven rectilinear locomotion systems.[10,25] This implies that to see in the s direction, the progressive motion of the vibration-driven system is similar to the rectilinear motion. The term $m(\ddot{\xi}_1+\ddot{\xi}_2)$ denotes the active force, and Q_ξ is the resistance. The system has periodic net displacement in the progressive direction due to the existence of anisotropic Coulomb dry friction Q_ξ.

2.2.2. Lateral motion.

$$(M+2m)\,\ddot{n}+2m\left(\dot{\xi}_1+\dot{\xi}_2\right)\dot{\theta}+m\left(\xi_1+\xi_2\right)\ddot{\theta}=Q_\eta. \tag{7}$$

From Eq. (7), one can see that the lateral motion is induced by the rotation of the system due to the terms containing $\dot{\theta}$ and $\ddot{\theta}$.

2.2.3. Turning motion.

$$\left(J+\sum_{j=1}^{2}m_j\left(\xi_j^2+B_j^2\right)-\tfrac{m}{M+2m}m(\xi_1+\xi_2)^2\right)\ddot{\theta}+\tfrac{\mathrm{d}}{\mathrm{d}t}\left(J+\sum_{j=1}^{2}m_j\left(\xi_j^2+B_j^2\right)-\tfrac{m}{M+2m}m(\xi_1+\xi_2)^2\right)\dot{\theta}$$
$$=mb\left(\ddot{\xi}_1-\ddot{\xi}_2\right)+M_\theta-\tfrac{m}{M+2m}\left(\xi_1+\xi_2\right)Q_\eta, \tag{8}$$

From the term $mb(\ddot{\xi}_1-\ddot{\xi}_2)$ in Eq. (8), one can easily see that the rotation motion of the system is mainly induced by the relative motions of the two internal masses. Specifically, if let $\xi_1(t)=\xi_2(t)$, which means the two internal masses perform a synchronized vibration, then $mb(\ddot{\xi}_1-\ddot{\xi}_2)=0$. It is known that friction is dependent on active force; if there is no active force, then the corresponding friction will vanish too. Thus, under initial condition $\dot{\theta}(0)=0$, the right-hand side of Eq. (8) is 0. Then, the latter two friction terms on the right-hand side of Eq. (8) are also equal to 0. Thus, Eq. (8) is reduced to

$$\left(J+\sum_{j=1}^{2}m_j\left(\xi_j^2+B_j^2\right)-\frac{m}{M+2m}m(\xi_1+\xi_2)^2\right)\ddot{\theta}=0, \tag{9}$$

from which one may solve that $\dot{\theta}(t)=0$ for the initial condition $\dot{\theta}(0)=0$ and θ can be an arbitrary constant value. This implies that the system never changes its direction under this situation. Furthermore, substituting $\dot{\theta}(t)=0$ into Eq. (5), one can obtain that

$$(M+2m)\,\ddot{x}+m\left(\ddot{\xi}_1+\ddot{\xi}_2\right)=Q_x. \tag{10}$$

It implies that under the condition $\xi_1=\xi_2$ with $\dot{\theta}(0)=0$, the planar locomotion system is degenerated into a rectilinear one. This is the criterion used to tell what kind of locomotion the robot will perform.

https://doi.org/10.1017/S0263574718000383 Published online by Cambridge University Press

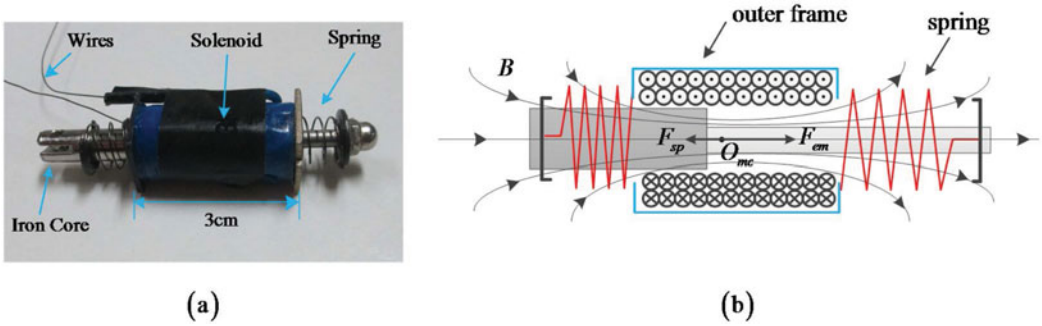


Fig. 3. (a) Photo of the electromagnet in *Shell*. (b) Periodic motion of the iron core (mass centre O_{mc}) are induced by periodic magnetic field force F_{em} and elastic spring force F_{sp}.

In the next section, a prototype—the minirobot *Shell*—is fabricated out to experimentally demonstrate the planar locomotion.

3. Robot Design and Prototype

In earthworm locomotion, earthworms periodically change their body shapes by muscle extensions and contractions. The muscle extension and contraction rate determines the locomotion speed of the worm. Meanwhile, earthworms will anchor themselves with the ground to prevent backward motion, manifesting as an extreme case of anisotropic dry friction. Accordingly, the driving frequency of internal oscillators and dry friction coefficients are critical to the design of the miniature robot. In this section, by emphasizing the two key components, actuation oscillator and anisotropic support, the fabrication of *Shell* is illustrated.

3.1. Actuation oscillators

The actuation of *Shell* is implemented by electromagnets (as shown in Fig. 3). The iron core is ferromagnetic, a property that allows it, when exposed to electrical current, to function as an electromagnet. Solenoids are devices capable of changing electrical energy into mechanical energy. When the insulated, coiled wire of the solenoid receives electrical current, the magnetic field produced by the coiled wire attracts the iron core (plunger). The plunger, which is connected to two springs, will overcome spring elasticity and strike into the coil. When the electric current is removed, the springs will pull the plunger back towards its original position. In this way, if the current applied to the coil is periodic, the plunger will vibrate along the magnetic field inside the hollow wire.

According to Ampere's law, magnetic field intensity of the solenoid shown in Fig. 3(b) is

$$B = \mu_0 NI/l, \tag{11}$$

where μ_0 is the magnetic constant, N the number of loops, I the current, and l the length of the wrapped coil. Assuming that the magnetic induction intensity B is uniformly distributed over pole face S, then according to Maxwell's formula, electromagnetic attraction can be expressed as[29]

$$F_{em} = B^2 \cdot S/2\mu_0. \tag{12}$$

From Eqs. (11) and (12), it is easy to see that electromagnetic attraction exciting the plunger by the magnetic field is constant for the steady current I applied to the coil. Specifically, suppose that the electric signal applied to the coil is a periodic square wave with a duty ratio of 50%. Correspondingly, electromagnetic attraction acting on the plunger is shown in Fig. 4(b). The aim of the applied current is to excite the plunger to vibrate harmonically within the magnetic field.

Up to now, the actuation of the vibration-driven locomotion system shown in Fig. 1 is boiled down to the dynamic response of two mass-spring oscillators (as shown in Fig. 4(a)) under periodic square

https://doi.org/10.1017/S0263574718000383 Published online by Cambridge University Press

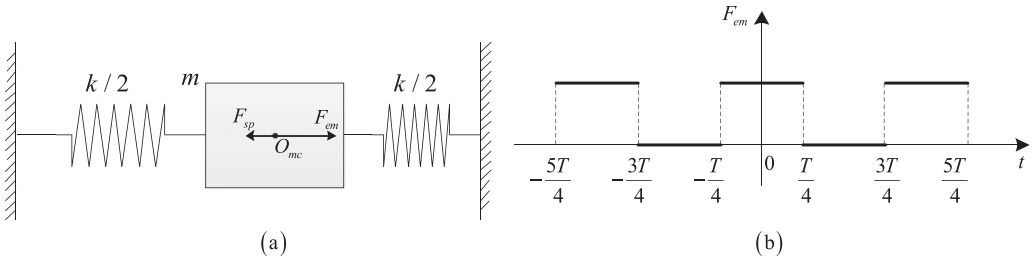


Fig. 4. (a) Dynamic model of the electromagnet shown in Fig. 3. (b) Periodic excitation of electromagnetic attraction produced by a direct current with a duty ratio of 50%.

wave excitation as

$$F_{em}(t) = \begin{cases} F_0, & t \in \left(nT - \frac{T}{4}, nT + \frac{T}{4}\right) \\ 0, & t \in \left(nT - \frac{T}{2}, nT - \frac{T}{4}\right) \cup \left(nT + \frac{T}{4}, nT + \frac{T}{2}\right) \end{cases}, \quad n = 1, 2, 3, \ldots. \tag{13}$$

With the help of Fourier expansion, $F(t)$ can also be expressed in series as

$$F_{em}(t) = \frac{F_0}{2} + \frac{2F_0}{\pi} \sum_{n=1,3,5,\ldots}^{\infty} \frac{1}{n}(-1)^{\frac{n-1}{2}} \cos n\Omega t, \tag{14}$$

where $\Omega = 2\pi/T$ is the excitation frequency. By regarding the damping as a small quantity and omitting it, we can write the governing equation of the oscillator shown in Fig. 4(a) as

$$m\ddot{\gamma} + k\gamma = F_{em}(t), \tag{15}$$

where γ is the displacement of the plunger, m the mass of oscillator, and $k/2$ the stiffness of each spring.

The solution of Eq. (15) is

$$\gamma(t) = \frac{2F_0}{\pi k} \sum_{n=1,3,5\cdots}^{\infty} \beta_n cosn\Omega t + \frac{F_0}{2k}, \tag{16}$$

where the amplitude amplification factor is $\beta_n = (-1)^{\frac{n-1}{2}}/(n|(1 - n^2\varpi^2)|)$, the frequency ratio $\varpi = \Omega/\omega_0$, and the natural frequency of the oscillator $\omega_0 = \sqrt{k/m}$.

It is easy to find that $|\bar{\beta}(n)|$ decreases as n grows. Besides,

$$\frac{|\beta_n|}{|\beta_1|} = \left|\frac{(-1)^{\frac{n-1}{2}}}{n\left(1 - n^2\varpi^2\right)}\right| \Big/ \left|\frac{(-1)^{\frac{1-1}{2}}}{1\left(1 - 1^2\varpi^2\right)}\right| = \frac{1}{n}\left|\frac{1 - \varpi^2}{(1 - n^2\varpi^2)}\right| \tag{17}$$

with $|\beta_n|/|\beta_1| \xrightarrow{\varpi \to 1} 0$ implying that the rest terms of the solution (16) are sufficiently small compared to its first term. Thus, it is reasonable to truncate the solution (16) into the first order as

$$\gamma(t) = \frac{2F_0}{\pi k}\frac{1}{1 - \varpi^2} cos\Omega t + \frac{F_0}{2k}, \tag{18}$$

which is simple harmonic. To move the robot, the actuation force provided by the two internal oscillators should be larger than at least the forward friction, i.e.,

$$(m_1 + m_2)\frac{2F_0}{\pi k}\frac{\Omega^2}{1 - \varpi^2} > \mu_\xi^+ (M + m_1 + m_2)\, g, \tag{19}$$

https://doi.org/10.1017/S0263574718000383 Published online by Cambridge University Press

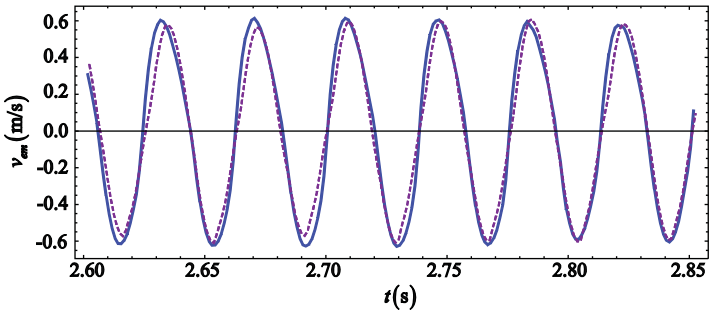


Fig. 5. Velocity time history of the two plungers under the electric current of frequency 25.5 Hz and voltage 24.0 V.

where μ_ξ^+ is the friction coefficient the robot subject to when moving forward.

Moreover,

$$\frac{F_0}{2k} \Big/ \left(\frac{2F_0}{\pi k} \frac{1}{1-\varpi^2} \right) = \frac{\pi \left(1-\varpi^2\right)}{4} \xrightarrow{\varpi \to 1} 0. \tag{20}$$

Generally, driving frequencies are selected near the natural frequency so that the driving force provided by the oscillators can be large enough to actuate the planar motion system. Thus, the constant term $F_0/2k$ in Eq. (18) is small such that it can be neglected here. Then, we conclude that the law of the two electromagnetic solenoids in the planar locomotion system fabricated can be expressed as

$$\xi_j(t) = A_j \sin\left(\omega_j t + \varphi_j\right), \ (j = 1, 2), \tag{21}$$

where A_j, ω_j, and φ_j are the driving amplitude, frequency, and phase applied to the jth internal mass, respectively. The following is a time history of the velocity of the plungers, as shown in Fig. 5. The plot is measured by a Polytec scanning vibrometer.

3.2. Anisotropic support

Under harmonic actuations, the locomotion of vibration-driven system depends on anisotropic external friction. In this paper, to provide the anisotropic friction, especially designed supports C_i (i =1, 2, 3, 4) are assembled at each of the four corners (as shown in Figs. 1 and 6). The support looks like a blade with one edge an arc of a certain radius r_s and the other edge perpendicular to the supporting plane. When the support moves forward or backward in the plane of uniform roughness, the edge will function as a probe or profilometer[30] to detect the asperity of the surface. Thus, with the stylus tip of different radius (the radius of the right sharp edge can be viewed as infinitely small), the plane will present different asperities. However, anisotropic friction will not show in the lateral motion due to its symmetric shape of the support in the η direction. It is easy to see that *Shell* only requires friction anisotropicity in the advancing direction (ξ) just as that in the rectilinear motion systems, so its design is as simple as the rectilinear ones in terms of the anisotropic friction. Furthermore, the friction anisotropicity always presents only in the heading direction (the positive ξ) of the robot. In this way, though the supporting plane is isotropic in friction, the friction *Shell* subject to can always be anisotropic due to the effect of the supports C_i (i =1, 2, 3, 4).

Two electromagnets, symmetric to each other, are clamped by two pieces of PMMA splints from above and below, as shown in Fig. 6. That is the reason why it is called *Shell*. Then, the robot is fixed tightly by five nylon bolts with one in the centre and four at the corners. The central one is mainly used to pull the two PMMA splints together so that the solenoids will have no relative displacement and the other four to finely adjust the levels of the four supports as well as to fasten. The red marker is used to locate *Shell* in the meshed plane.

https://doi.org/10.1017/S0263574718000383 Published online by Cambridge University Press

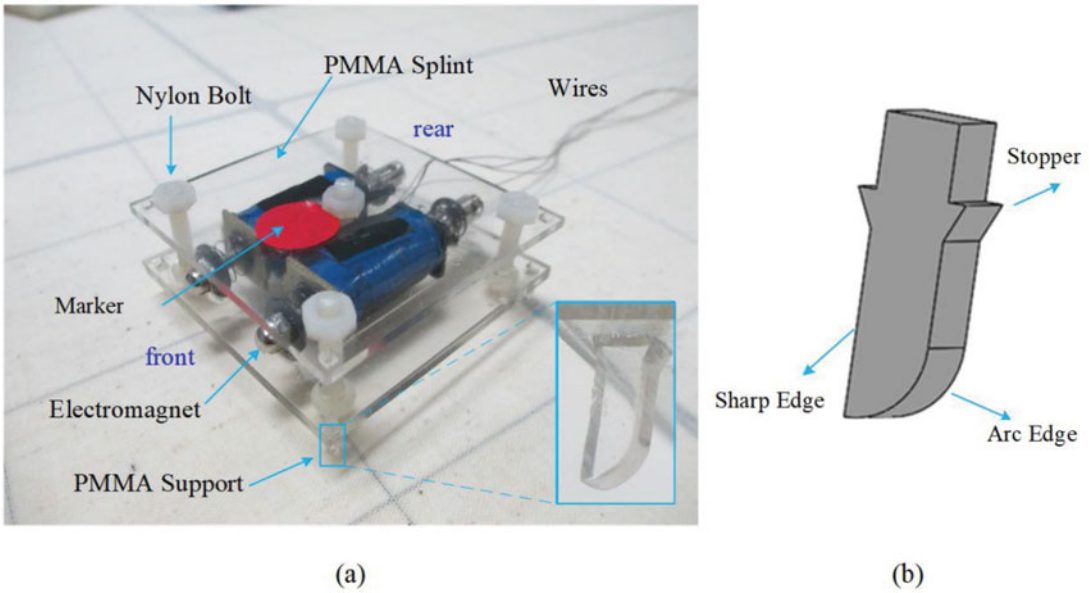


Fig. 6. (a) Structure of *Shell* and an enlarged support can be seen at the lower right corner. (b) 3D model of the support made of PMMA of length 7.8 mm; the radius of the arc edge is 2.1 mm.

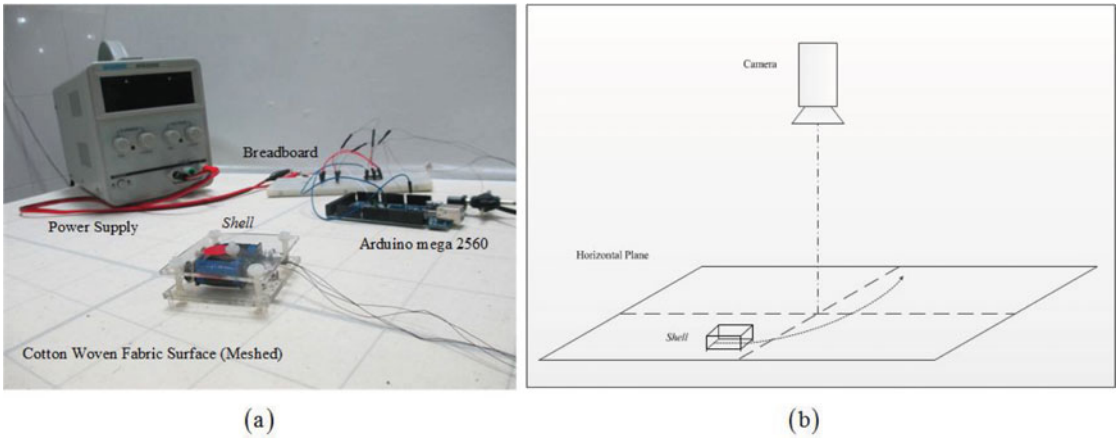


Fig. 7. (a) Experiment setup: *Shell*, power supply, control circuit, and horizontal plane. (b) Scheme of video recording of planar trajectory of *Shell*.

4. Locomotion Tests

In this section, to show the manoeuvrability of *Shell,* the robot is controlled to perform different kinds of planar locomotion. The behaviour of *Shell* is directed by adjusting the frequencies of its internal drives. To do this, first, the setup of the experiment is introduced.

4.1. Experimental setup and parameter identification

The power of the robot *Shell* is supplied by a constant current power source, and the electric current signal is controlled by Arduino mega 2560, with which the frequency of the electric current is controlled. The horizontal rough plane with grids on is covered by cotton woven fabric to provide proper friction (as shown in Fig. 7(a)). Speed and direction of *Shell* can be altered by changing the internal frequencies through serial port communication.

A camera is placed right above the centre of the horizontal plane (as shown in Fig. 7(b)) to record the locomotion history of *Shell* (as shown in Fig. 8). When *Shell* is powered on to move around on the rough plane, videos of its locomotion processes will be created. Then, with the aid of the red marker, the planar trajectory of *Shell* can be identified by image identification.

https://doi.org/10.1017/S0263574718000383 Published online by Cambridge University Press

Table I. Friction coefficients for the support moving towards different directions.

Forward	Backward	Laterally
0.570	0.628	0.602

Table II. Values of physical parameters.

Physical parameters	Values
Total mass of *Shell* (g)	64.4
Mass of a single iron core, m (g)	8.3
Stiffness of a single spring, $k/2$ (N/m)	100.2
Mass of single electromagnet (g)	21.1
Acceleration of gravity, g (m/s^2)	9.8
Half of the longitudinal length, a (mm)	30.0
Half of the transverse length, d (mm)	30.0
Half of the distance between two drives, b (mm)	10.5
Length of the solenoid (mm)	30.0
Width of the solenoid (mm)	13.0
Total rotational inertia, J (kg $\cdot$ m^2)	1.646×10^{-5}

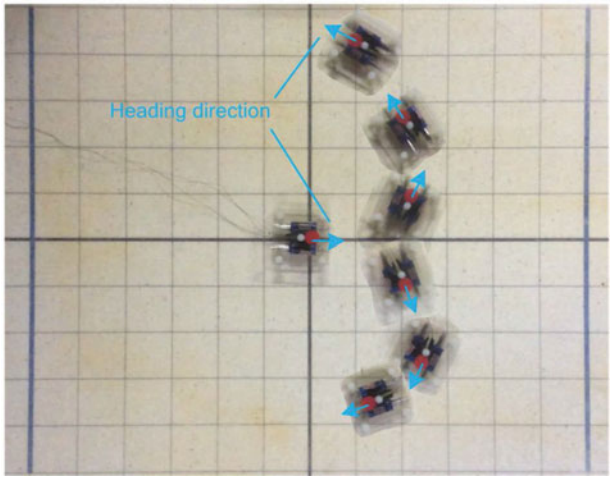


Fig. 8. Robot turning clockwise and anticlockwise due to driving frequencies swapped.

Friction coefficients are measured by pulling the robot to move at a steady speed. The friction coefficients are listed in Table I.

Other physical parameters of the experimental prototype are listed in Table II.

Numerical results are simulated based on the theoretical analysis in Section 2 with physical parameters shown in Table II. In the following content, we compare numerical results with the experimental ones in terms of planar trajectories of *Shell*.

4.2. 2D locomotion trajectories

Following the procedures presented above, different kinds of planar trajectories of *Shell* are recorded and identified as follows.

4.2.1. Circles. Figure 9 shows two circle trajectories of *Shell*. Both trajectories (bc and ba) are performed experimentally for three times and plotted in the red disk, green square, and blue rhombus, respectively. They are sampled from *Shell*'s trajectories at a frequency of 30 frames a dot. The circle in dashed line is fitted from the three experimental trajectories and the average radius is taken. The circle in dot line is the simulated result through the dynamical model proposed in Section 1 with the 4th-order Runge–Kutta method. Specifically, in Fig. 9(bc), the driving frequencies (as shown in

https://doi.org/10.1017/S0263574718000383 Published online by Cambridge University Press

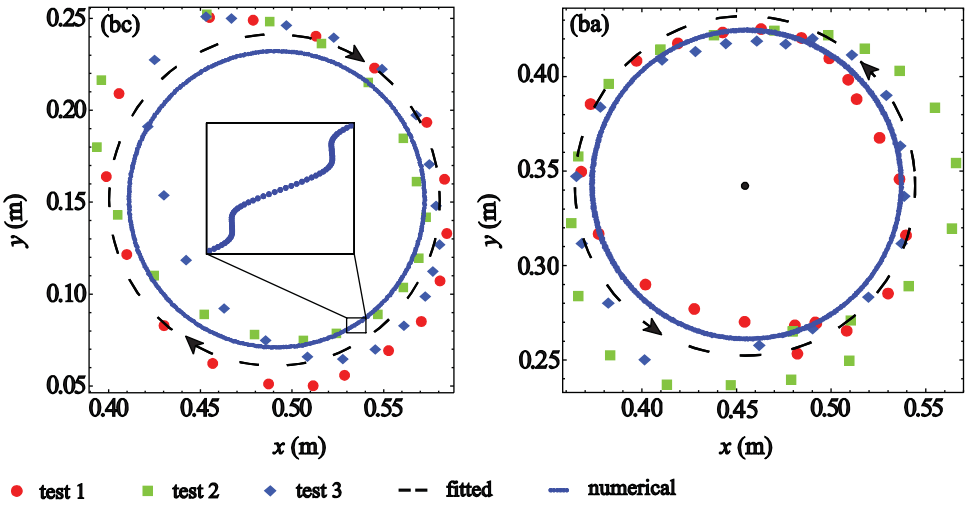


Fig. 9. Two circular trajectories of *Shell*; each experiment is performed for three times and denoted by dots of different colours and shapes; the fitting circle is in dashed line and the numerical one is in dots; the directions of the robot are denoted by arrows; an enlarged view of the simulated trajectory is shown in the centre of (bc).

Eq. (21)) are $f_1 = 27.0$ Hz ($f_i = \omega_i/2\pi$) (for the mass m_1 on the left side of *Shell*) and f_2 =24.0 Hz (for the right mass m_2). The two excitation frequencies are chosen near the natural frequency (24.7 Hz) of the oscillators such that large propulsion force can be provided. Physical parameters of the design of the oscillators can be referred to in Table II. Correspondingly, the amplitudes measured by the Polytec scanning vibrometer are $A_1 = 3.4$ mm and $A_2 = 1.1$ mm. From the drives, one may see that the inertial force amplitude $A_1\omega_1^2$ provided by the mass m_1 is larger than that of m_2. This force disparity may result in a clockwise torque applied to the robot and it is driven to turn clockwise. A segment of the simulated trajectory is zoomed in to show the detail of the locomotion. In fact, the robot oscillates periodically, but from the macro-view, it moves along a circle with a certain radius. The radii of the fitted and simulated circle are 90.1 mm and 84.0 mm, respectively, and the relative error is 6.82%. The linear and angular speeds of *Shell* in Fig. 9(bc) are 24.6 mm/s and 0.27 rad/s, respectively.

By swapping the driving frequency of the two internal drives, i.e., in the case of $f_1 = 24.0$ Hz and $f_2 = 27.0$ Hz with A_1 =1.0 mm and $A_2 = 3.3$ mm, we plot the experimental and numerical results in Fig. 9(ba). Amplitudes A_1 and A_2 are slightly different from those in the bc case due to the inevitable manufacturing error. In this case, the robot turns anticlockwise. The radii of the fitted and simulated circle are 89.9 mm and 85.1 mm, respectively, and the relative error is 5.34 %. The linear and angular speeds of *Shell* in Fig. 9(ba) are 24.6 mm/s and 0.27 rad/s, respectively. The radii and speed are close to those in the case of bc.

Similarly, Fig. 10 is plotted under another set of driving frequencies. In Fig. 10(sc), the driving frequencies are f_1 =25.5 Hz and f_2 =22.5 Hz, and the corresponding amplitudes are $A_1 = 4.2$ mm and $A_2 = 0.1$ mm. The radii of the fitted and simulated circle are 47.6 mm and 50.3 mm, respectively, and the relative error is 5.67 %. The linear and angular speeds of *Shell* in Fig. 10(sc) are 23.0 mm/s and 0.48 rad/s, respectively. In Fig. 10(sa), the driving frequencies are $f_1 = 22.5$ Hz and $f_2 = 25.5$ Hz, and the corresponding amplitudes are $A_1 = 0.9$ mm and $A_2 = 4.1$ mm. The radii of the fitted and simulated circle are 43.5 mm and 48.5 mm, respectively, and the relative error is 11.38 %. The linear and angular speeds of *Shell* in Fig. 10(sa) are 21.0 mm/s and 0.48 rad/s, respectively. Compared to the bc and ba cases, the radii and linear speeds in sc and sa cases are smaller, but the robot turns in faster speeds. The radii and speed are also close to those in the case of sc.

4.2.2. Straight lines. In Section 2.2.3, we conclude that under the condition $\xi_1 = \xi_2$ with $\dot{\theta}(0) = 0$, the planar locomotion system will degenerate into a rectilinear one. This is the criterion in choosing the driving parameters to achieve rectilinear or circular locomotion of the robot. According to this, by setting the driving frequencies of mass m_1 and m_2 equal, we obtain approximate straight line trajectories of the robot. The applied frequency is 27.0 Hz, and the corresponding amplitudes are $A_1 =$

https://doi.org/10.1017/S0263574718000383 Published online by Cambridge University Press

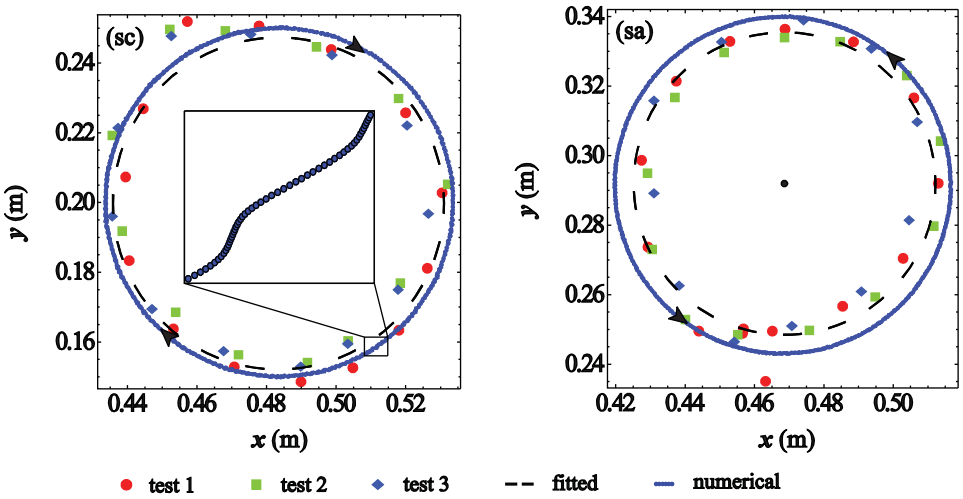


Fig. 10. Circle trajectories with driving frequencies 25.5 Hz and 22.5 Hz.

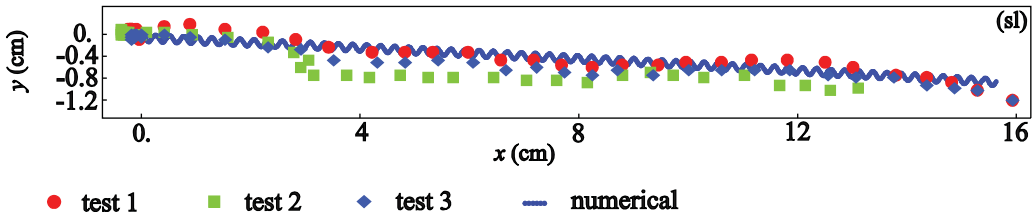


Fig. 11. Straight line trajectories with $f_1 = f_2 = 27.0$ Hz and $A_1 = 3.6$ mm and $A_2 = 3.3$ mm; the red, green, and blue dot lines are experimental results and the solid line is numerical.

3.6 mm and $A_2 = 3.3$ mm. A slight difference is observed in the amplitudes of the two oscillators. This is due to the inevitable error in the fabrication of the two electromagnets though they are applied by exactly the same signal. The difference will lead to the driving force disparity of the robot. However, for the torque is tiny, the radius of the circular trajectory is large. Thus, the trajectories shown in Fig. 11 are in fact tiny segments of large circles. Locally, we can regard them as straight lines with a slight inclination. The linear speed of *Shell* in Fig. 11 is about 30.2 mm/s. This case is denoted as sl.

By synthesizing the five cases above, we plot part of the trajectories together in Fig. 12. As predicted in Section 2.2.1, trajectories in cases sc and sa are symmetric to each other about the straight line sl. The only difference between the two cases is the direction of turning, i.e., the sign of $\dot{\theta}$ in Eq. (5), is the opposite. This is apparently because the frequency swap and the robot always turns to the side with the smaller driving force amplitude. Essentially, the robot *Shell* produces turning motion due to this kind of driving force disparity. As a special case, if the driving forces provided by the two internal oscillators are exactly the same, then the robot will move along a straight line. Furthermore, Fig. 12 also implies that the radius of circular trajectories could be continuously adjusted by changing the driving frequencies of the two internal masses.

4.2.3. Walk around obstacles. To verify the repeatability of the planar locomotion of *Shell*, an '∞' type planar trajectory is performed by controlling it to move around two obstacles for three loops, denoted by red, green, and blue, respectively, in Fig. 13. The state of the robot is shifted between cases bc and ba, and the shifts only happen within the shaded ellipse region. Thus, it is an open loop control by simply swapping the driving frequencies of the two internal masses. Table III lists out all the information of the locomotion in different stages.

4.2.4. A free walk. Finally, a free walk of *Shell* in the horizontal plane is given, as shown in Fig. 14. It is a combination of straight lines and curves. Red points on the planar trajectories denote the potions where driving parameters are changed.

https://doi.org/10.1017/S0263574718000383 Published online by Cambridge University Press

Table III. Driving parameters of *Shell* in each stage in walking around obstacles.

Stages	Duration (s)	Turning	f_1 (Hz)	f_2 (Hz)	Radius (mm)	Speed (mm/s)
1	10.9	Anticlockwise	24.0	27.0	131.0	37.5
2	24.5	Clockwise	27.0	24.0	108.3	29.4
3	22.7	Anticlockwise	24.0	27.0	103.2	30.7
4	23.5	Clockwise	27.0	24.0	109.2	26.7
5	24.3	Anticlockwise	24.0	27.0	102.0	30.0
6	29.5	Clockwise	27.0	24.0	108.1	24.6
7	14.2	Anticlockwise	24.0	27.0	88.9	26.7

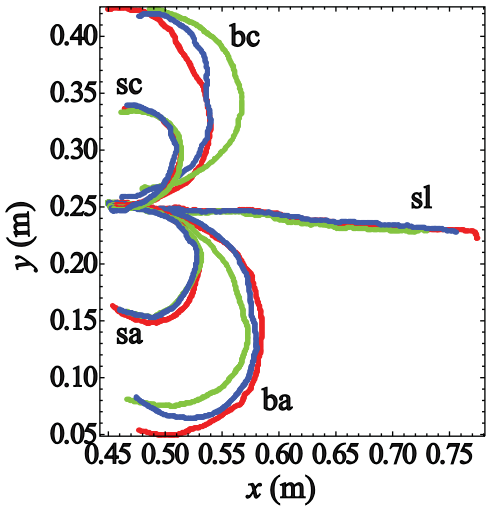


Fig. 12. Comparison of trajectories with the driving frequency varying.

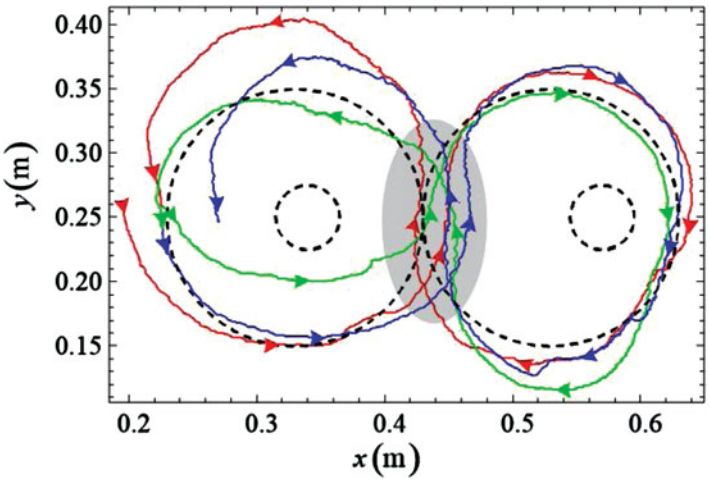


Fig. 13. An '∞' type planar trajectory performed around two circular obstacles; the two small dashed circles denoting the two actual obstacles in experiment and the two big dashed circles are the fitted circles of the curve trajectories.

4.3. Discussion

From the above experimental results, one may find that *Shell* can moves flexibly on the plane, but errors still exist. Through the experiment, we conclude that the error between the experimental and numerical results mainly lies in the following aspects:

1. Transient processes lie in the beginning stage and result from the driving parameter shifting.
2. The roughness of the supporting plane may not be uniformly distributed.

https://doi.org/10.1017/S0263574718000383 Published online by Cambridge University Press

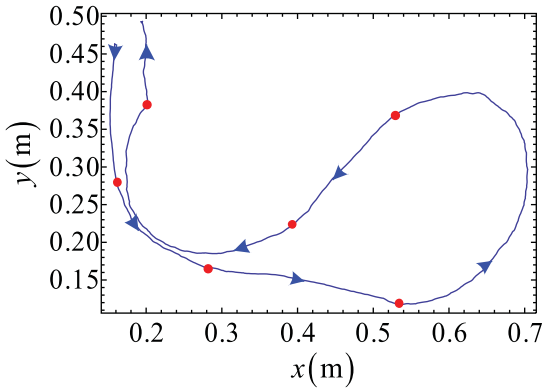


Fig. 14. A free walk of *Shell*; driving parameters are changed at the red points.

3. Magnetic field variation of the electromagnets induced by thermal changes.

5. Conclusions

In this paper, a parallel-drive based minirobot *Shell* is designed and prototyped based on vibration-driven locomotion mechanism. The robot can not only move rectilinearly at a speed of 30.2 mm/s but also perform circular locomotion with different radii. Based on this, more generic planar trajectories can be constructed by controlling the frequencies of the two internal drives in *Shell*. Main results of our work are listed as follows:

1. To move the robot, blade-like supports are designed to provide anisotropic dry friction. This is our first goal. Furthermore, the friction anisotropicity is only shown in the advancing direction of the robot, which makes the friction design relatively simple. Different pairs of the blade radius and the contact surface roughness can provide different anisotropicity of dry friction. Thus, the optimal pair of the support and the contact surface is another meaningful work both in locomotion realization and in friction or contact investigation.
2. With the simple friction design, our second goal is how to make the robot turn freely on the horizontal plane. To this end, we propose the idea of disparity in the driving forces of the robot. Experimentally, we can set the frequencies of the parallel internal drives different from each other so that an active torque can be produced to rotate the robot.
3. Governing equations of the planar locomotion of the robot are given in the natural coordinates, from which one may easily see that the advancing motion of the planar locomotion is similar to the rectilinear motion under the condition of small angular speed and the angular motion of the robot is mainly induced by the inertial forces of the two internal masses.
4. Rectilinear and circular trajectories can both be performed by *Shell*, based on which the procedure of the locomotion robot can be tailored. Then, *Shell* can be controlled to move freely in the horizontal plane to perform tasks like obstacle avoidance.
5. Numerical simulation is performed based on theoretical analysis. Numerical trajectories of straight lines and circles agree well with the experimental ones. Explanations are given for the errors between theoretical predicted and experimental results.

The idea of advance disparity is fundamental and easily embedded in designing various locomotion systems except for vibration-driven systems. This kind of planar locomotion can be easily controlled (generally only one driving parameter is enough) to move along arcs of various curvatures. Thus, the work here gives some hint in modelling planar locomotion systems. In addition, the blade-like supports illustrated here are novel and demonstrated to be effective in providing anisotropic dry friction. With these two essential designs, the planar locomotion vibration-driven robot can be modelled almost as simple as the ones that can only perform rectilinear locomotion.

The content of the paper is the first step in exploration of the robot. The future work would be optimization of the robot in turning radius, speed and energy consumption, aiming at improving the accuracy and efficiency of the robot locomotion. In addition, the robot presented in this paper is

https://doi.org/10.1017/S0263574718000383 Published online by Cambridge University Press

mainly modelled and designed to move in a horizontal plane. Extending its working environment to unstructured 3D space would be a challenging and meaningful work for practical application of the locomotion robot.

Acknowledgment

We thank Mr. Zuolin Liu for extensive discussions and assistance in experiments that were of great value to this work. This research was supported by the National Natural Science Foundation of China under Grant no. 11572224.

Supplementary materials

To view supplementary material for this article, please visit https://doi.org/10.1017/S0263574718000383.

References

1. K. Karydis, Y. Liu, I. Poulakakis and H. G. Tanner, "A template candidate for miniature legged robots in quasi-static motion," *Auton. Robot.* **38**(2), 193–209 (2015).
2. A. A. Transeth, K. Y. Pettersen and P. Liljebäck, "A survey on snake robot modeling and locomotion," *Robotica* **27**(7), 999–1015 (2009).
3. P. Liljebäck, K. Y. Pettersen, O. Stavdahl and J. T. Gravdahl, *Snake Robots: Modelling, Mechatronics, and Control* (Springer, London, 2012).
4. K. Wang, G. Yan, G. Ma and D. Ye, "An earthworm-like robotic endoscope system for human intestine: Design, analysis, and experiment," *Ann. Biomed. Eng.* **37**(1), 210–221 (2009).
5. H. T. Lin, G. G. Leisk and B. Trimmer, "GoQBot: A caterpillar-inspired soft-bodied rolling robot," *Bioinspir. Biomim.* **6**(2), 026007 (2011).
6. J. J. Yao, S. Gao, G. L. Jiang, T. L. Hill, H. Yu and D. Shao, "Screw theory based motion analysis for an inchworm-like climbing robot," *Robotica* **33**(8), 1704–1717 (2015).
7. C. Li, C. C. Kessens, A. Young, R. S. Fearing and R. J. Full, "Cockroach-Inspired Robot Reveals Principles of Ground-Based, Dynamic Self-Righting," *Proceedings of the IEEE/RSJ International Conference on Intelligent Robots and Systems (IROS 2016)*, Daejeon, South Korea, 2016, pp. 2128–2134.
8. N. N. Bolotnik, I. M. Zeidis, K. Zimmermann and S. F. Yatsun, "Dynamics of controlled motion of vibration-driven systems," *J. Comput. Syst. Sci. Int.* **45**(5), 831–840 (2006).
9. N. N. Bolotnik and T. Y. Figurina, "Optimal control of the rectilinear motion of a rigid body on a rough plane by means of the motion of two internal masses," *PMM – J. Appl. Math. Mech.* **72**(2), 126–135 (2008).
10. F. L. Chernousko, "Analysis and optimization of the motion of a body controlled by means of a movable internal mass," *PMM – J. Appl. Math. Mech.* **72**(6), 819–842 (2006).
11. F. L. Chernousko, "On the optimal motion of a body with an internal mass in a resistive medium," *J. Vib. Control* **14**(1–2), 197–208 (2008).
12. K. Zimmermann, I. Zeidis and C. Behn, *Mechanics of Terrestrial Locomotion: With a Focus on Non-Pedal Motion Systems* (Springer, Berlin, 2009).
13. H. B. Fang and J. Xu, "Dynamics of a mobile system with an internal acceleration-controlled mass in a resistive medium," *J. Sound Vibr.* **330**(16), 4002–4018 (2011).
14. T. Y. Figurina, "Optimal control of system of material points in a straight line with dry friction," *J. Comput. Syst. Sci. Int.* **46**(2), 227–233 (2007).
15. H. B. Fang and K. W. Wang, "Piezoelectric vibration-driven locomotion systems – Exploiting resonance and bistable dynamics," *J. Sound Vibr.* **391**, 153–169 (2016).
16. H. Li, K. Furuta and F. L. Chernousko, "A Pendulum-Driven Cart Via Internal Force and Static Friction," *Proceedings of the International Conference on Physics and Control*, Saint Petersburg, Russia, 2005, pp. 15–17.
17. H. Li, K. Furuta and F. L. Chernousko, "Motion Generation of the Capsubot Using Internal Force and Static Friction," *Proceedings of the 45th IEEE Conference on Decision and Control*, San Diego, USA, 2006, pp. 6575–6580.
18. Y. Liu, E. Pavlovskaia and M. Wiercigroch, "Experimental verification of the vibro-impact capsule model," *Nonlinear Dyn.* **83**(1), 1029–1041 (2015).
19. H. B. Fang, S. Y. Li, K. W. Wang and J. Xu, "A comprehensive study on the locomotion characteristics of a metameric earthworm-like robot: Part A: Modelling and gait generation," *Multibody Syst. Dyn.* **34**(4), 391–413 (2015).
20. S. Hasanzadeh and A. A. Tootoonchi, "Ground adaptive and optimized locomotion of snake robot moving with a novel gait," *Auton. Robot.* **28**(4), 457–470 (2010).
21. S. Hirose and A. Morishima, "Design and control of a mobile robot with an articulated body," *Int. J. Robot. Res.* **9**(2), 99–114 (1990).

https://doi.org/10.1017/S0263574718000383 Published online by Cambridge University Press

22. D. Zarrouk and R. S. Fearing, "Controlled in-plane locomotion of a hexapod using a single actuator," *IEEE Trans. Robot.* **31**(1), 157–167 (2015).
23. C. W. Song, D. J. Lee and S. Y. Lee, "Bioinspired segment robot with earthworm-like plane locomotion," *J. Bionic Eng.* **13**(2), 292–302 (2016).
24. M. Arai, Y. Tanaka, S. Hirose, H. Kuwahara and S. Tsukui, "Development of "Souryu-IV" and "Souryu-V:" Serially connected crawler vehicles for in-rubble searching operations," *J. Field Robot.* **25**(1–2), 31–65 (2008).
25. H. B. Fang and J. Xu, "Stick-slip effect in a vibration-driven system with dry friction: Sliding bifurcations and optimization," *J. Appl. Mech. – Trans. ASME* **81**(5), 51001 (2014).
26. H. B. Fang and J. Xu, "Dynamics of a three-module vibration-driven system with non-symmetric Coulomb's dry friction," *Multibody Syst. Dyn.* **27**(4), 455–485 (2012).
27. C. Behn and K. Zimmermann, "Adaptive λ-tracking for locomotion systems," *Robot. Auton. Syst.* **54**(7), 529–545 (2006).
28. L. Y. Volkova and S. F. Yatsun, "Simulation of the plane controlled motion of a three-mass vibration system," *J. Comput. Syst. Sci. Int.* **51**(6), 859–878 (2012).
29. L. Mei, J. Liu and Z. Fu, "Calculation of electromagnet attractive force and simulation analysis," *Micromotors* **45**(6), 6–9 (2012).
30. R. Gohar and H. Rahnejat, *Fundamentals of Tribology* (Imperial College Press, London, 2012).

Appendix: Governing Equations of Planar Locomotion

To obtain kinematic energy of the vibration-driven system, we denote $\mathbf{r}_1$ as the position vector of the ith mass in rectangular coordinate system xoy, $\mathbf{oo}_1 = (x, y)^{\mathrm{T}}$ as that of body M 's centre, $\mathbf{o_1p_i}$ as that of mass m_i $(i = 1, 2)$, as shown in Fig. 15. Then, one has

$$\mathbf{r}_i = \mathbf{oo}_1 + \mathbf{o}_1\mathbf{p}_i, \quad (i = 1, 2)\,, \tag{A1}$$

where $\mathbf{o}_1\mathbf{p}_1 = T_r \cdot (\xi_1, b)^{\mathrm{T}}$, $\mathbf{o}_1\mathbf{p}_2 = T_r \cdot (\xi_2, -b)^{\mathrm{T}}$ in xoy with the transform matrix

$$T_r = \begin{pmatrix} \cos\theta & -\sin\theta \\ \sin\theta & \cos\theta \end{pmatrix}. \tag{A2}$$

It is easily seen that kinematic energy of the ith mass is expressed as

$$T_i = m_i\dot{\mathbf{r}}_i^2/2 + J_i\dot{\theta}^2/2, \quad (i = 1, 2)\,, \tag{A3}$$

where J_i is the moment of inertia of the ith mass with respect to its own centre, and

$$\dot{\mathbf{r}}_i = \begin{pmatrix} \dot{x}_i \\ \dot{y}_i \end{pmatrix} = \begin{pmatrix} \dot{x} - \xi_i\dot{\theta}\sin\theta - B_i\dot{\theta}\cos\theta + \dot{\xi}_i\cos\theta \\ \dot{y} + \xi_i\dot{\theta}\cos\theta - B_i\dot{\theta}\sin\theta + \dot{\xi}_i\sin\theta \end{pmatrix}. \tag{A4}$$

Here, $B_i = (-1)^{i+1}b$ for brevity. Substituting Eqs. (A1) and (A2) into (A3) yields

$$\begin{aligned} T_i = m_i \Big[&\left(\dot{x} - \xi_i\dot{\theta}\sin\theta - B_i\dot{\theta}\cos\theta + \dot{\xi}_i\cos\theta\right)^2 \\ &+\left(\dot{y} + \xi_i\dot{\theta}\cos\theta - B_i\dot{\theta}\sin\theta + \dot{\xi}_i\sin\theta\right)^2\Big]/2 + J_i\dot{\theta}^2/2, \quad (i = 1, 2)\,. \end{aligned} \tag{A5}$$

Similarly, kinematic energy of body M is given by

$$T_0 = m_0(\dot{x}^2 + \dot{y}^2)/2 + J_0\dot{\theta}^2/2, \tag{A6}$$

where $m_0 = M$ and J_0 is the moment of inertia of body M with respect to its centre. Thus, the total kinematic energy of the system considered can be expressed as

$$T = \sum_{i=0}^{2} T_i. \tag{A7}$$

https://doi.org/10.1017/S0263574718000383 Published online by Cambridge University Press

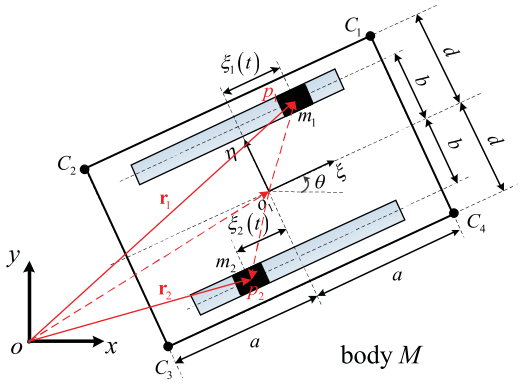


Fig. 15. Kinematic diagram of planar locomotion robot.

By using Lagrange's equation of the second kind on Eq. (A7), the governing equations of the motion of the vibration-driven system are derived, as shown in Eq. (1). However, friction forces and torque Q_x, Q_y, and M_θ cannot be obtained directly for the lack of the velocity and normal pressure at each support C_i $(i = 1, 2, 3, 4)$, which determine the direction and magnitude of Coulomb friction. The absolute velocity of the centre of body M is $V_{o1} = (\dot{x}, \dot{y})^{\mathrm{T}}$ obtained by differentiating the position vector $\mathbf{oo}_1 = (x, y)^{\mathrm{T}}$ to time t. Similarly, its angular velocity is $\dot{\theta}$. It is noted that friction anisotropicity exists only in the direction of ξ, i.e., the forward and backward directions of body M. Thus, to determine the Coulomb friction body M subject to, we need to express absolute velocities at each support C_i $(i = 1, 2, 3, 4)$ in the coordinates system of $\xi o_1 \eta$

$$\begin{aligned}
\mathbf{V}_1 &= \left(\dot{x}\cos\theta + \dot{y}\sin\theta - d\dot{\theta}\right)\mathbf{e}_1 + \left(\dot{y}\cos\theta - \dot{x}\sin\theta + a\dot{\theta}\right)\mathbf{e}_2 \\
\mathbf{V}_2 &= \left(\dot{x}\cos\theta + \dot{y}\sin\theta - d\dot{\theta}\right)\mathbf{e}_1 + \left(\dot{y}\cos\theta - \dot{x}\sin\theta - a\dot{\theta}\right)\mathbf{e}_2 \\
\mathbf{V}_3 &= \left(\dot{x}\cos\theta + \dot{y}\sin\theta + d\dot{\theta}\right)\mathbf{e}_1 + \left(\dot{y}\cos\theta - \dot{x}\sin\theta - a\dot{\theta}\right)\mathbf{e}_2 \\
\mathbf{V}_4 &= \left(\dot{x}\cos\theta + \dot{y}\sin\theta + d\dot{\theta}\right)\mathbf{e}_1 + \left(\dot{y}\cos\theta - \dot{x}\sin\theta + a\dot{\theta}\right)\mathbf{e}_2
\end{aligned} \tag{A8}$$

Noting that some components of $\mathbf{V}_i$ $(i = 1, 2, 3, 4)$ are the same, we can thus reduce formula (A8) into the following form:

$$\begin{aligned}
\mathbf{V}_1 &= V_{11}\mathbf{e}_1 + V_{12}\mathbf{e}_2 \\
\mathbf{V}_2 &= V_{11}\mathbf{e}_1 + V_{22}\mathbf{e}_2 \\
\mathbf{V}_3 &= V_{41}\mathbf{e}_1 + V_{22}\mathbf{e}_2 \\
\mathbf{V}_4 &= V_{41}\mathbf{e}_1 + V_{12}\mathbf{e}_2
\end{aligned} \tag{A9}$$

where $\mathbf{e}_1$ and $\mathbf{e}_2$ are unit vectors along the positive ξ and η axes, respectively

$$\begin{aligned}
V_{11} &= \dot{x}\cos\theta + \dot{y}\sin\theta - d\dot{\theta} \\
V_{12} &= \dot{y}\cos\theta - \dot{x}\sin\theta + a\dot{\theta} \\
V_{22} &= \dot{y}\cos\theta - \dot{x}\sin\theta - a\dot{\theta} \\
V_{41} &= \dot{x}\cos\theta + \dot{y}\sin\theta + d\dot{\theta}
\end{aligned} \tag{A10}$$

It implies that half of the components, i.e., four of them can completely determine absolute velocities at each support C_i $(i = 1, 2, 3, 4)$.

To figure out dry friction, normal pressure should be known first. Normal pressure N_i $(i = 1, 2, 3, 4)$ at each support C_i $(i = 1, 2, 3, 4)$ is statically indeterminate, that is, there are only three equations about them that are not enough to work out all four normal pressures. However, from the following discussion, one may find that in fact, there is no need to solve every normal pressure N_i $(i = 1, 2, 3, 4)$ to determine resistances Q_x, Q_y, and M_θ. Assuming that the four supports never lose contacts with the rough supporting plane, based on the conditions of static equilibrium one may derive the equations

https://doi.org/10.1017/S0263574718000383 Published online by Cambridge University Press

concerning normal pressures at supports that

$$\begin{cases} N_1 + N_2 + N_3 + N_4 = (M + 2m)\, g \\ 2d\,(N_1 + N_2) = (d + b)\, mg + (d - b)\, mg + Mgd \\ 2d\,(N_3 + N_4) = (d + b)\, mg + (d - b)\, mg + Mgd \\ 2a\,(N_1 + N_4) = (a + \xi_1\,(t))\, mg + (a + \xi_2\,(t))\, mg + aMg \\ 2a\,(N_2 + N_3) = (a - \xi_1\,(t))\, mg + (a - \xi_2\,(t))\, mg + aMg \end{cases}, \tag{A11}$$

or in another form as

$$\begin{cases} N_1 + N_2 = N_3 + N_4 = (M + 2m)\, g/2 \\ N_1 + N_4 = (M + 2m)\, g/2 + [\xi_1\,(t) + \xi_2\,(t)]\, mg/2a \\ N_2 + N_3 = (M + 2m)\, g/2 - [\xi_1\,(t) + \xi_2\,(t)]\, mg/2a \end{cases}. \tag{A12}$$

Thus, from Eq. (A12), it is easy to see that resistances Q_ξ, Q_η, and M_θ can be uniquely determined. Q_x and Q_y can then be expressed with the help of transform matrix

$$\begin{pmatrix} Q_x \\ Q_y \end{pmatrix} = T_r \cdot \begin{pmatrix} Q_\xi \\ Q_\eta \end{pmatrix} = \begin{pmatrix} \cos\theta & -\sin\theta \\ \sin\theta & \cos\theta \end{pmatrix} \cdot \begin{pmatrix} \sum_{i=1}^{4} Q_{\xi i} \\ \sum_{i=1}^{4} Q_{\eta i} \end{pmatrix} = \begin{pmatrix} \cos\theta \sum_{i=1}^{4} Q_{\xi i} - \sin\theta \sum_{i=1}^{4} Q_{\eta i} \\ \sin\theta \sum_{i=1}^{4} Q_{\xi i} + \cos\theta \sum_{i=1}^{4} Q_{\eta i} \end{pmatrix}. \tag{A13}$$

Here, we let anisotropic dry friction coefficients in the ξ direction

$$\mu_\xi\,(V_i) = \begin{cases} -\mu_\xi^+, & V_{i\xi} > 0 \\ \mu_\xi^-, & V_{i\xi} < 0 \end{cases}, \tag{A14}$$

where $V_{i\xi}$ is the absolute velocity of the ith support in the ξ direction; μ_ξ^+ and μ_ξ^- are positive dry friction coefficients. To move the vibration-driven system forward, it is assumed that

$$\mu_\xi^+ < \mu_\xi^-, \tag{A15}$$

which implies friction anisotropicity in the ξ direction. Dry friction coefficients in the η direction is given as

$$\mu_\eta\,(V_i) = \begin{cases} -\mu_\eta, & V_{i\eta} > 0 \\ \mu_\eta, & V_{i\eta} < 0 \end{cases}, \tag{A16}$$

which shows that the friction coefficients in the η direction are isotropic and μ_η is positive. Then, the Coulomb dry friction in the ξ direction can be obtained as

$$\begin{aligned} Q_\xi &= \sum_{i=1}^{4} \mu_\xi\,(\mathbf{V}_i \cdot \mathbf{e}_1) N_i \\ &= \mu_\xi\,(V_{11})\, N_1 + \mu_\xi\,(V_{11})\, N_2 + \mu_\xi\,(V_{41})\, N_3 + \mu_\xi\,(V_{41})\, N_4 \\ &= \mu_\xi\,(V_{11})\,(N_1 + N_2) + \mu_\xi\,(V_{41})\,(N_3 + N_4) \\ &= \begin{cases} -\mu_\xi^+\,(m_0 + m_1 + m_2)\, g, & V_{11} > 0 \text{ and } V_{41} > 0 \\ \left(-\mu_\xi^+ + \mu_\xi^-\right)(m_0 + m_1 + m_2)\, g/2, & V_{11} > 0 \text{ and } V_{41} < 0 \\ \left(-\mu_\xi^+ + \mu_\xi^-\right)(m_0 + m_1 + m_2)\, g/2, & V_{11} < 0 \text{ and } V_{41} > 0 \\ \mu_\xi^-\,(m_0 + m_1 + m_2)\, g, & V_{11} < 0 \text{ and } V_{41} < 0 \end{cases}. \end{aligned} \tag{A17}$$

https://doi.org/10.1017/S0263574718000383 Published online by Cambridge University Press

Similarly,

$$\begin{aligned} Q_\eta &= \sum_{i=1}^{4} \mu_\eta \left(\mathbf{V}_i \cdot \mathbf{e}_2\right) N_i \\ &= \begin{cases} -\mu_\eta \left(m_0 + m_1 + m_2\right) g, & V_{12} > 0 \text{ and } V_{22} > 0 \\ -\mu_\eta \left(\xi_1 + \xi_2\right) mg/a, & V_{12} > 0 \text{ and } V_{22} < 0 \\ \mu_\eta \left(\xi_1 + \xi_2\right) mg/a, & V_{12} < 0 \text{ and } V_{22} > 0 \\ \mu_\eta \left(m_0 + m_1 + m_2\right) g, & V_{12} < 0 \text{ and } V_{22} < 0 \end{cases}, \end{aligned} \tag{A18}$$

and

$$\begin{aligned} M_\theta &= \sum_{i=1}^{4} \mathbf{o}_1\mathbf{C}_i \times \left(\mu_\xi \left(\mathbf{V}_i \cdot \mathbf{e}_1\right) \mathbf{e}_1 + \mu_\eta \left(\mathbf{V}_i \cdot \mathbf{e}_2\right) \mathbf{e}_2\right) N_i \\ &= \sum_{i=1}^{4} \begin{vmatrix} \mathbf{e}_1 & \mathbf{e}_2 & \mathbf{k} \\ \mathbf{o}_1\mathbf{C}_i \cdot \mathbf{e}_1 & \mathbf{o}_1\mathbf{C}_i \cdot \mathbf{e}_2 & 0 \\ \mu_\xi \left(\mathbf{V}_i \cdot \mathbf{e}_1\right) & \mu_\eta \left(\mathbf{V}_i \cdot \mathbf{e}_2\right) & 0 \end{vmatrix} N_i \\ &= \sum_{i=1}^{4} \left[\left(\mathbf{o}_1\mathbf{C}_i \cdot \mathbf{e}_1\right) \mu_\eta \left(\mathbf{V}_i \cdot \mathbf{e}_2\right) - \left(\mathbf{o}_1\mathbf{C}_i \cdot \mathbf{e}_2\right) \mu_\xi \left(\mathbf{V}_i \cdot \mathbf{e}_1\right)\right] N_i \mathbf{k} \\ &= \sum_{i=1}^{4} \left[\left(\mathbf{o}_1\mathbf{C}_i \cdot \mathbf{e}_1\right) \mu_\eta \left(\mathbf{V}_i \cdot \mathbf{e}_2\right) - \left(\mathbf{o}_1\mathbf{C}_i \cdot \mathbf{e}_2\right) \mu_\xi \left(\mathbf{V}_i \cdot \mathbf{e}_1\right)\right] N_i \mathbf{k}, \end{aligned} \tag{A19}$$

where $\mathbf{k}$ is the unit vector along the axis z and

$$\mathbf{o}_1\mathbf{C}_1 = (a, d), \quad \mathbf{o}_1\mathbf{C}_2 = (-a, d), \quad \mathbf{o}_1\mathbf{C}_3 = (-a, -d), \quad \mathbf{o}_1\mathbf{C}_4 = (a, -d). \tag{A20}$$

Here, the stick-slip effect is not taken into consideration.

https://doi.org/10.1017/S0263574718000383 Published online by Cambridge University Press